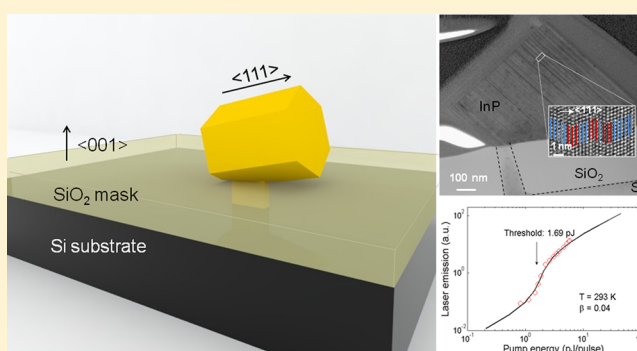


Polytypic InP Nanolaser Monolithically Integrated on (001) Silicon

Zhechao Wang,^{†,‡} Bin Tian,^{†,‡} Mohanchand Paladugu,[§] Marianna Pantouvaki,[§] Nicolas Le Thomas,^{†,‡} Clement Merckling,[§] Weiming Guo,[§] Johan Dekoster,[§] Joris Van Campenhout,[§] Philippe Absil,[§] and Dries Van Thourhout^{*,†,‡}[†]INTEC Department, Ghent University, Sint-Pietersnieuwstraat 41, Ghent 9000, Belgium[‡]Center for Nano- and Biophotonics (NB-Photonics), Ghent University, Sint-Pietersnieuwstraat 41, Ghent 9000, Belgium[§]IMEC, Kapeldreef 75, 3001 Heverlee, Belgium

Supporting Information

ABSTRACT: On-chip optical interconnects still miss a high-performance laser monolithically integrated on silicon. Here, we demonstrate a silicon-integrated InP nanolaser that operates at room temperature with a low threshold of 1.69 pJ and a large spontaneous emission factor of 0.04. An epitaxial scheme to grow relatively thick InP nanowires on (001) silicon is developed. The zincblende/wurtzite crystal phase polytypism and the formed type II heterostructures are found to promote lasing over a wide wavelength range.



KEYWORDS: Nanolaser, selective area metal–organic vapor-phase epitaxy, InP, polytypism, silicon photonics, optical interconnects

The convergence of photonics and electronics holds promises for many applications. Optical interconnect is envisioned to be a competitive solution for overcoming the intra- and interchip communication bottleneck that now threatens to limit the performance of next-generation microprocessors.^{1–3} The underlying technology has evolved tremendously over the past decade; however, a high performance on-chip laser source is still missing, and that triggered a vast amount of research across the world.^{4–8} Although extensive work is being carried out nowadays to engineer silicon or germanium to provide gain,^{4,7,8} compared to their III–V counterparts, silicon or germanium lasers are still in their infancy. A possible approach to integrate III–V materials on silicon involves wafer bonding techniques.^{5,6} A monolithic approach would be more appealing, but its implementation is difficult due to the intrinsic lattice and thermal mismatch between silicon and III–Vs.⁹ Nevertheless considerable progress has recently been made. While the optimization of large-area growth of III–Vs on silicon is under way,^{10–13} localized epitaxial approaches, for example, the growth of III–V nanowires on silicon (albeit mostly on the (111) surface), have shown remarkable progress.^{14–17} To achieve lasing from these nanowires, a complex cleavage and transfer process is usually employed to form the Fabry–Perot laser cavity.^{18–20} The resulting low yield and high cost make this approach less attractive for practical applications. Recently, laser operation of GaAs/InGaAs nanowires that were directly grown on a (111) silicon substrate was reported.²¹ Growth of these nanowires was initiated from a surface roughing process. Nevertheless

there is a need for a more controllable growth scheme. Besides, the use of (001) oriented substrates is preferable, considering its potential compatibility with processing in standard microelectronics fabs.

In this work, we present a more controllable scheme for growing InP nanowire lasers on prepatterned (001) silicon substrates using a metal–organic chemical vapor deposition process (MOCVD). A nanotrench assisted defect-trapping effect²² is thereby exploited in combination with an epitaxial lateral overgrowth²³ process to promote the growth of thick but high quality InP nanowires on silicon, well-suited for photonic applications. High-resolution transmission electron microscopy (HRTEM) analysis revealed that wurtzite (WZ) and zincblende (ZB) crystal phases are mixed in the nanowire, forming type II heterostructures. Although it was suggested that the twins and stacking faults formed between different crystal phases may degrade the optical performance,²⁴ in this work, we found that the crystal phase mixture actually act as an efficient staggered quantum well system. A low threshold room-temperature laser operation is successfully achieved. We also measured a high spontaneous emission factor β indicating that a large fraction of the spontaneous emission is coupled into the resonant optical mode,²⁵ which contributes to reducing the laser threshold.

Received: June 13, 2013

Revised: September 15, 2013

Published: September 27, 2013

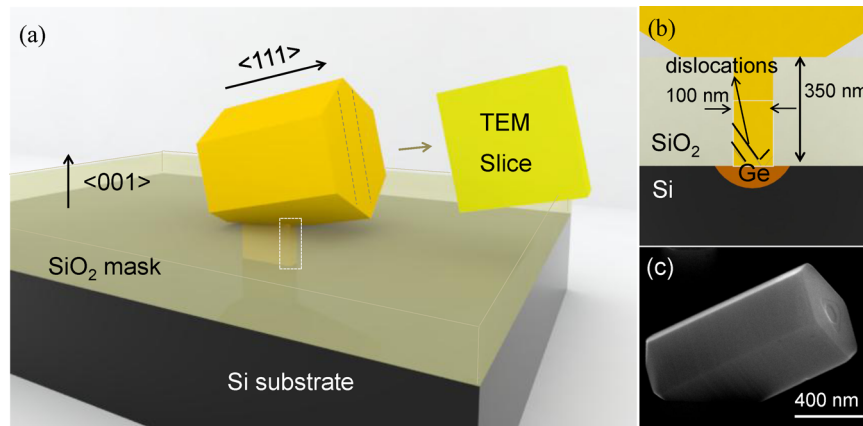


Figure 1. (a) A schematic configuration of the InP nanolaser epitaxially grown on (001) silicon; the dashed lines indicate that a slice of the nanocavity is prepared for transmission electron microscopy (TEM) analysis. (b) A cross-section view of the nanowire bottom (see the dashed rectangle in part a) that is connected to the silicon substrate via a SiO₂ opening and the Ge buffer. (c) A tilted scanning electron microscopy (SEM) view of a typical nanolaser cavity.

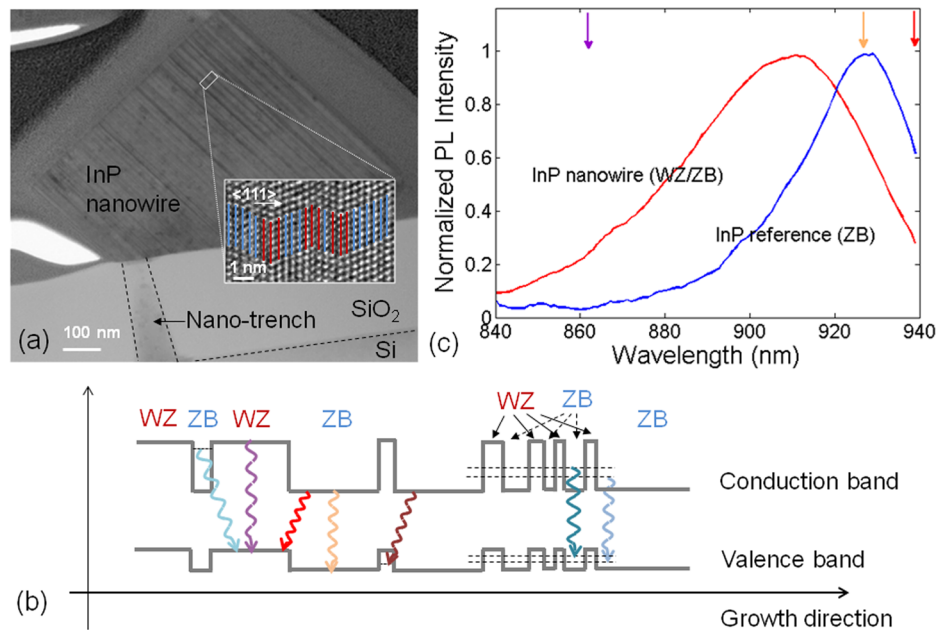


Figure 2. (a) Transmission electron microscopy (TEM) image of InP nanowire. Dashed lines are used to outline the InP-filled SiO₂ trench, which is not clearly observable due to the misalignment of the FIB prepared slice with respect to the nanowire center. Insert: High-resolution TEM image of a small fraction of the wurtzite/zincblende mixed InP nanowire, blue and red lines are used to represent the atomic planes of ZB and WZ crystal phases, respectively. (b) Schematics of the band alignment in the WZ/ZB mixed nanowire. Different arrows represent different possible carrier transitions, and the dashed lines indicate the possible energy levels of the quantum confined carriers. (c) Normalized PL spectra measured from the InP nanowire sample (red) and the InP reference sample (blue). The red, yellow, and purple arrows indicate the type II, the pure ZB, and the pure WZ band edge transition, respectively.

Most of the previously demonstrated III–V nanowires grown on silicon had lateral dimensions in the order of tens of nanometers,^{14,26} limited by the huge lattice mismatch (4–8%) between the substrate and the nanowires. Such thin nanowires can hardly sustain any confined optical modes and therefore cannot act as a laser cavity. We used an alternative approach whereby the epitaxial growth begins selectively within 100 nm diameter sized circular openings that are defined in a 350 nm thick SiO₂ mask on (001) silicon substrates (see insert of Figure 1a). A modified shallow trench isolation (STI) process also used in standard CMOS fabrication is used to fabricate this patterned SiO₂ mask.²⁷ The silicon surface in these patterned openings is etched away using HCl at high temperature (600

°C) in a CVD reactor. Subsequently, a thin Ge seed layer is grown in the recessed Si holes to reduce the lattice mismatch. Epitaxial growth was carried out in a MOCVD reactor. Initially, the wafer was baked in a H₂ flow at high temperature (650 °C). This high temperature process not only removes the native oxide but also forms surface steps on the Ge surface that facilitate InP nucleation without the generation of anti phase boundaries (APBs).²² Different from the conventional approach that uses miscut substrates, this Ge seed based scheme is compatible with (001) oriented substrates also used in standard CMOS fabrication. In the next step, the temperature was lowered to 380 °C, following introduction of low flow rates of the reactants *tert*-butyl phosphine (TBP)

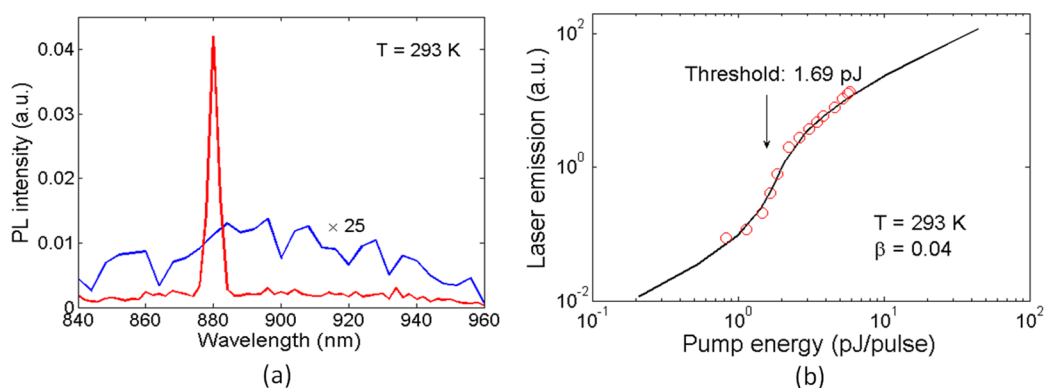


Figure 3. Laser oscillation of InP nanolaser grown on silicon. (a) PL emission spectra recorded below (blue) and above (red) the threshold. The blue curve was measured at 60% of the threshold pump level, and it has been magnified by $\times 25$ for better visibility. (b) L–L curve of a nanolaser operating at room temperature; the open circles are measured results, while the solid curve is the corresponding rate equation fitting. The threshold is measured to be as low as 1.69 ± 0.2 pJ. From rate equation fitting, a spontaneous emission factor of 0.04 was extracted.

and trimethylindium (TMI) for the InP nucleation. Subsequently, the reactant flow rates were increased in small increments, while the temperature was being increased to 610 °C. Dislocations that propagate from the lattice mismatched interface glide along certain angles with respect to the bottom surface. By increasing the aspect ratio of the holes (depth/diameter > 2), all of the dislocations will be annihilated at the sidewalls (see insert of Figure 1a), and defect-free InP can be obtained at the SiO₂ hole top surface, which then can be treated as a lattice matched virtual substrate for the subsequent epitaxial process. In this way, one gets rid of the constraint of the critical diameter,²⁸ and the lateral dimensions of the InP nanowires can be increased considerably, employing an epitaxial lateral overgrowth process. As shown in Figure 1a, the subsequent epitaxial growth above the mask surface forms a nanowire with a hexagonal cross-section in a diameter of about 400 nm, its longitudinal axis tilted about 35° with respect to the mask surface. A scanning electron microscopy (SEM) image of a typical InP/Si nanowire optical cavity is shown in Figure 1b. The nanowire growth is oriented along the $\langle 111 \rangle$ axis, which is mainly determined by the lower surface energy of the side facets. A hexagonal top surface and an inner triangular pattern can be seen in the SEM image and is routinely found in all of the SEM observations. We believe this morphology originates from the temperature changes during the nucleation and growth steps, which affect the crystal planes forming the wire sidewalls.²⁹ It is worthwhile mentioning that this epitaxy process was originally developed for realizing III-Vs based logic devices in a CMOS fab.²² Its potential CMOS compatibility makes it very attractive for mass volume applications requiring dense integration with advanced electronics.

Using a focused ion beam (FIB) a ~ 100 nm thick slice of the nanowire (see Figure 1a) was prepared for transmission electron microscopy (TEM) analysis. From the TEM inspection, no dislocations can be found, which confirms the efficiency of the defect trapping effect. The InP nanowire mainly consists of the ZB crystal phase, with twin planes found to be randomly distributed along the axial direction. A twin plane punched into the ZB InP can be considered as a monolayer of WZ InP. Also thicker layers of WZ InP are observed. A high-resolution TEM image illustrating this crystal phase mixture is shown in Figure 2a. Blue and red lines represent the atomic planes of the ZB and WZ phases, respectively. According to theoretical prediction and exper-

imental verification, WZ InP exhibits an 80 meV larger bandgap than ZB InP,^{30,31} and the “heterostructure” formed by the two crystal phases of InP shows a type II^{32,33} alignment; that is, the conduction band minimum and valence band maximum are not in the same layer. Therefore the electron and hole wave functions are spatially separated.

Although the nanowire is too thick to provide quantum confinement in the lateral direction, the finite thickness of the WZ and ZB segments (see Figure 2a) provide quantum confinement in the other direction. Figure 2b shows a schematic band diagram of the polytypic nanowire. Due to the type II band alignment at the WZ/ZB interface, the effective bandgap shrinks, and the corresponding PL emission is red-shifted (see the red arrow). However, when a thin WZ (ZB) segment is sandwiched between relatively wide ZB (WZ) segments, an isolated quantum well is formed (see the left side of the diagram). Theoretical calculations show that, even for a wide quantum well (~ 10 nm), the ground state for electrons is still 50 meV above the well bottom.³³ Therefore the bandgap shrinkage related to the type II band alignment can be compensated or even exceeded. In the case of a few monolayer thick segments, the quantum states will be further lifted up (see the blue arrow)^{32,33} approaching the top of the well,^{32,33} and carriers may escape and enter the above-barrier continuum states at room temperature. The corresponding PL emission is further blue-shifted (see the purple arrow). Note that, due to the narrow width of the quantum wells, the weakly confined electron and hole wave functions overlap strongly in real space, and therefore the direct carrier transition is greatly enhanced. The theoretically predicted and experimentally measured decrease of radiative lifetime presented in ref 32 also supports this hypothesis. In the case of closely packed WZ/ZB segments (see the right side of the diagram), a nonperiodic superlattice is formed.^{34,35} The resultant electronic states are better confined compared with the single quantum well case, which reduces the chance of carrier leakage to continuum states.³⁵ The delocalization of the carrier wave functions is further increased in the real space, greatly enhancing the radiative recombination rate.

Figure 2c shows a typical PL spectrum recorded from nanowires at room temperature. The pumping area covered hundreds of nanowires. The PL spectrum measured from a reference sample (a pure InP wafer) under the same conditions is also plotted. Compared with the reference sample, the InP/Si

PL spectrum is considerably blue-shifted, with its peak position on the left side of the ZB band edge transition (see the yellow arrow). This measurement result indicates that the dominant carrier transition process happens between different quantum states as discussed above, and the quantum confinement effects are strong enough to overcome the PL red shift due to the type II band alignment (its corresponding band edge transition is marked by the red arrow). On the other hand, we observed very low PL signals above the WZ InP bandgap (see the purple arrow), indicating that only a few carriers can escape and enter into the above-barrier continuum states. In addition, due to the inhomogeneous distribution of the WZ/ZB heterostructures with different segment thicknesses, the spontaneous emission spectrum is rather wide. We will show later that, for different optical cavity dimensions, the lasing wavelength can be tuned across the whole spectral range.

From these cavities, room temperature laser operation is achieved through optical pumping with a Nd:YAG nanosecond pulsed laser (Ekspla, 532 nm, repetition rate 321 Hz). Pump pulses with a 7 ns length were attenuated before being delivered to the sample surface by a $\times 50$, 0.6 numerical aperture (NA) objective (Mitutoyo NIR HR). The optical setup allows a uniform and size adjustable pump pattern on the sample surface. PL emission at room temperature was collected by the objective used for optical pumping and detected through a 1/4 m monochromator (MS257, Newport) by a TE-cooled silicon detector. Filters were used to block the pumping light in the PL collecting path. The signal was locked to the pump via a lock-in amplifier to improve the signal-to-noise ratio for measurements below threshold. To minimize the interference from the neighboring nanowires, the pumping area was reduced to a diameter of about 3 μm .

The typical PL spectra of a nanowire laser, recorded below and above threshold (pump intensity >3 times threshold level), are plotted in Figure 3a. The below-threshold emission spectrum is magnified by a factor 25 for better visibility. Although this spectrum stems from a single nanowire, it is rather broad and is centered around 890 nm, which indicates the strong quantum confinement effects and the nonuniform distribution of the WZ/ZB heterostructures over the nanowire. By increasing the pump intensity, a resonant mode starts to build up, and a laser peak located around 880 nm can be clearly identified (see the red curve). In contrast to conventional lasers, the measured line width of the nanowire laser is well above the Shawlow–Townes limit, and it remains almost constant (~ 2 nm) even when the pump intensity is increased considerably above threshold. Such a large discrepancy cannot be explained by the line width enhancement factor, which represents the line width enhancement through the amplitude–phase coupling mechanism of a semiconductor material. It has been found that, in a microcavity laser, the spontaneous emission rate and stimulated emission rate become comparable to the carrier equilibrium rate when the spontaneous emission factor β is large. The resulting nonequilibrium carrier distribution brings extra noise, and therefore the line width is enlarged.^{36,37} More lasing behavior characterization results, for example, the gain pinning (Figure S3) and a microscope image of the PL emission (Figure S4) can be found in the Supporting Information. The spontaneous emission spectra below threshold are provided in Figure S5, showing the evolution of the resonant mode below threshold. Although the signal-to-noise ratio is quite low, one can still distinguish the narrowing of the spectrum with increasing pumping level.

Figure 3b maps the InP/Si nanolaser room temperature emission power as function of the pump energy on a logarithmic scale. The clear discontinuity in the curve slope is a strong signature of a laser threshold. From a classic rate equations fitting of the measured results (solid curve in Figure 3b) we find a spontaneous emission factor $\beta = 0.04$, which indicates that a large part of the spontaneous emission is coupled into the laser mode. This large β is in line with the observed low laser threshold. The threshold is obtained by multiplying the pump intensity with the FDTD calculated nanowire's absorption cross-section, which is around $0.6 \times 10^{-12} \text{ m}^2$ at the pumping wavelength. The measured pumped intensity is comparable with the one previously demonstrated in ref 21.

As already discussed above, it is found that the nonuniformly distributed type II WZ/ZB heterostructures with different segment thicknesses emit photons covering a wide wavelength range (see Figure 2c). One could expect that such a broad band gain medium could be used to demonstrate wide wavelength tuning. In Figure 4, we plot the emission spectra measured

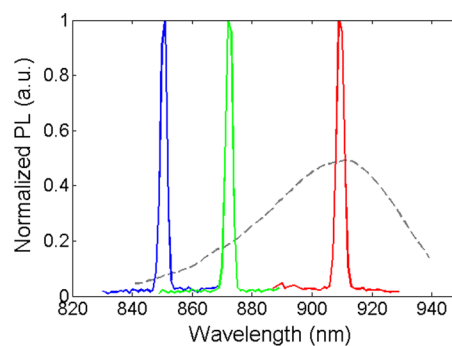


Figure 4. Above threshold PL spectra emitted from three different nanolasers are plotted. The below-threshold PL spectrum measured from the InP nanowire sample is also shown.

from three different InP/Si nanowire lasers (the spontaneous emission curve of Figure 2c is replotted here as a reference). Lasing over a range of 60 nm is achieved without material composition optimization. Further study of the threshold and spontaneous emission factor for lasers with different lasing wavelengths can be found in Figure S2. The small threshold variation for lasers having a similar lasing wavelength indicates that, although the gain medium is formed by a random mixture of crystal phases, the resultant gain spectrum does not change much from one laser to another.

As will be shown in a later section, the resonant wavelength is mainly determined by the lateral dimensions of the nanowire cavity. Therefore, by controlling the growth time, it is possible to fine-tune the lasing wavelength. We also found that the surroundings of the nanowire (local filling factor, failure of surrounding nanowires to grow) affects its dimensions and hence its lasing wavelength. This is believed to be caused by the loading effect of the epitaxial growth and provides another way to tune the wavelength, that is, by controlling the loading effect and the corresponding cavity dimensions by intentionally and carefully designing the surrounding mask pattern. In addition, it has been reported that the growth of different crystal phases can be controlled by optimizing the epitaxial growth conditions.^{34,35,38,39} This new bandgap engineering technique may further improve the nanowire laser performance by

matching the gain spectrum peak with the resonant optical mode.

It has to be stressed that the demonstrated low-threshold InP/Si laser consists purely of InP without any passivation layers or post surface treatments. The orders of magnitude lower surface recombination velocity of InP compared with other III-Vs, for example, GaAs, is believed to play an important role in the low-threshold room-temperature laser operation. Considering the simple fabrication procedure and its robustness over surface conditions, the demonstrated InP/Si laser may find its place in practical applications.

To identify the optical mode that oscillates in the nanowire cavity, simulations were performed by using commercial FDTD software (Lumerical). The cavity dimensions were measured directly through SEM inspection of the laser cavity shown in Figure 1c, whose measurement results can be found in Figure S6 (the lasing wavelength is located around 851 nm, and the spontaneous emission factor is extracted to be 0.03). The side edges of the hexagonal cross section and the cavity length are measured to be 245 nm and 1.4 μm , respectively. The tilt angle between the cavity axis and the substrate surface is 35.26°. To obtain a value for the refractive index of WZ InP, which is not directly available from literature, we used the Sellmeier equation⁴⁰ and the derived group index to perform a nonlinear curve fit to the measured WZ InP group index reported in ref 35. To take into account the nonuniform distribution of the two crystal phases along the nanowire, and considering that the thickness of the individual segments is much smaller than the working wavelength, we used an averaged refractive index for the whole cavity. By FDTD simulations, we found that all of the calculated optical modes belong to the helically propagating mode family that has six lobes at the cross section. Due to the missing corner of the nanowire at the bottom contact, no Fabry–Perot mode with a reasonably high Q factor was observed.

By analyzing the different resonant modes, we found that the mode with the highest Q factor has a resonant wavelength very close to the measured one. The calculated mode profile, assuming a 30% WZ/70% ZB composition for the nanowire, is shown in Figure 5. A helically propagating mode is identified.²¹ Its strong azimuthal components result in a hexagonal whispering-gallery (WG)-like mode pattern in the transversal plane (see Figure 5a), while its net mode propagation along the

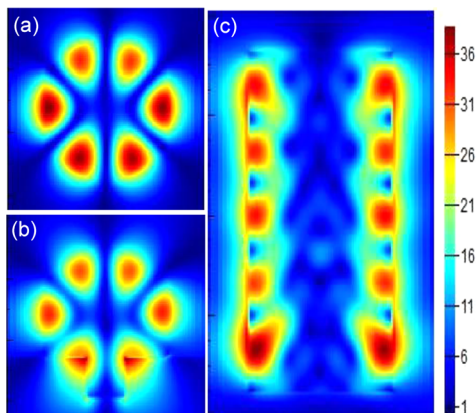


Figure 5. FDTD simulated mode profile of the laser cavity presented in Figure 3. (a, b) Cross-section views of the mode profile that are taken at the top and the bottom of the nanowire cavity. (c) Standing wave pattern of the optical mode along the nanowire axis.

nanowire axis forms a standing wave (see Figure 5b). In Figure 5c, we also plot the mode profile in the transversal direction at the bottom of the nanowire. It is found that the mode profile is not much disturbed by the direct contact with the SiO₂ mask, which proves the stability of the helical mode with respect to perturbations at the bottom facet side. By varying the WZ fraction in the simulated nanowire from 0% to 30%, the resonant wavelength shifts linearly from 850 to 860 nm, which agrees reasonably well with the experimentally recorded lasing wavelength (851 nm). The small discrepancy is believed to come from the inaccuracy of the SEM inspections. The cavity exhibits a relatively small cavity Q factor (120–150), and the calculated mode volume is around $2.5(\lambda/n)^3$. Simulation was also performed for the case of a perfect nanowire cavity—a complete hexagonal nanowire without silicon substrate (see Figure S1 in the Supporting Information). A one-order-of-magnitude-higher Q factor was found for the same resonant mode. Compared with the simulation results of the titled cavity, the pronounced effects of the tilt of the nanowire and its bottom contact with the substrate can be identified. Although it is difficult to grow a vertical nanowire on a (001) substrate, improvement of the Q factor by increasing the SiO₂ trench depth, and therefore reducing the downward leakage, is still an option to explore.

To explain the relatively large spontaneous emission factor β obtained, we start from its definition, the fraction of spontaneous emission radiated into the resonant mode:

$$\beta = \frac{F}{F + \alpha} \quad (1)$$

with F as the Purcell factor, denoting the spontaneous emission rate enhancement of an emitter placed in a cavity with respect to the free-space case. F can be expressed as:

$$F = \frac{3}{4\pi^2} \frac{\lambda}{\Delta\lambda} \frac{(\lambda_c/n)^3}{V_{\text{eff}}} \quad (2)$$

with V_{eff} and λ_c as the optical mode volume and the central wavelength of the cavity mode, respectively, n is the refractive index at the field maximum, and $\Delta\lambda$ is the larger of either the electron transition broadening or the cavity resonance line width. Given the relatively low cavity Q , the Purcell factor is estimated to be below 5 when the WZ fraction is tuned from 0% to 30% in simulations. In addition, considering the spatial, spectral, and polarization mismatch between the active medium and the resonant mode, the Purcell factor used in expression 1 should be replaced by an averaged spontaneous emission enhancement factor F_{ave} over the whole cavity.²⁵ Following the simple procedure presented in ref 25, F_{ave} is estimated close to 0.1. Therefore, the experimentally obtained high spontaneous emission factor does not originate from an extremely high Purcell factor.

On the other hand, from re-examining formula 1, one can derive that even in the case where F is small a large spontaneous emission factor can be obtained as long as α is sufficiently small. The parameter α represents the spontaneous emission that is coupled into the leaky modes and the nonlasing modes that spectrally overlap with the emitter:⁴¹ $\alpha = \zeta + \sum F_{\text{nonlasing}} F_{\text{nonlasing}}$ is the Purcell factor of the nonlasing modes. Considering the relatively large size of the cavity, the radiative emission rate into leaky modes is similar to the radiative rate in a homogeneous medium ($\zeta \approx 1$). On the other hand, from FDTD simulation we find 11 resonant modes that overlap with

the gain spectrum (800–1000 nm). Assuming the nonlasing modes have a similar averaged spontaneous emission enhancement factor ($F_{\text{nonlasing}}$) as the one calculated above for the lasing mode (F_{ave}), we can estimate α to be around 2, resulting in spontaneous emission factor β equal to 0.05, which agrees reasonably well with the experimental results. Therefore we can conclude that the large spontaneous emission factor mainly arises from the fact that only a limited number of resonant modes are supported by the small cavity.

In summary, we have demonstrated an InP nanolaser that operates at room temperature and can be selectively grown on a prepatterned (001) silicon substrate without any complex postprocessing. A unique epitaxial scheme combining the defect necking effect with a lateral overgrowth is used to grow a short but relatively thick nanowire cavity on silicon for photonic applications. The nanowires are found to consist of a mixture of ZB and WZ crystal phases. Although there is still discussion in literature whether the twins formed between the WZ and ZB InP crystal phases are optically active or not, the room-temperature laser operation presented here proves that WZ/ZB heterostructures can indeed function as an efficient gain medium. A wide gain spectrum is obtained from randomly distributed WZ/ZB heterostructures with different thicknesses. Furthermore, the compact size of the nanowire cavity limits the number of possible resonant modes, and a large spontaneous emission factor is experimentally demonstrated. Such a compact, robust, and silicon-integrated laser may play an important role in many application fields such as on-chip optical interconnects, biological sensing, and quantum information processing.

■ ASSOCIATED CONTENT

● Supporting Information

FDTD simulation of the ideal nanowire cavity, measurement results of a series of nanowire lasers, more characterization results of the nanowire laser, characterization results of the nanowire laser presented in Figure 1c. This material is available free of charge via the Internet at <http://pubs.acs.org>.

■ AUTHOR INFORMATION

Corresponding Author

*Address: Sint-Pietersnieuwstraat 41, 9000 Gent, Belgium. Phone: +32-9-264 3438. Fax: +32-9-264 3593. E-mail: dries.vanhourhout@intec.ugent.be.

Notes

The authors declare no competing financial interest.

■ ACKNOWLEDGMENTS

This work was supported through the EU ERC starting grant ULPPIC and the Belgian Science Policy Office (IAP P7/35-photonics@be).

■ REFERENCES

- (1) Chen, G.; Chen, H.; Haurylau, M.; Nelson, N. A.; Albonese, D. H.; Fauchet, P. M.; Friedman, E. G. *Integration, VLSI J.* **2007**, *40* (4), 434–446.
- (2) Miller, D. A. B. *Proc. IEEE* **2009**, *97* (7), 1166–1185.
- (3) Beausoleil, R. G.; Kuekes, P. J.; Snider, G. S.; Wang, S. Y.; Williams, R. S. *Proc. IEEE* **2008**, *96* (2), 230–247.
- (4) Rong, H.; Jones, R.; Liu, A.; Cohen, O.; Hak, D.; Fang, A.; Paniccia, M. *Nature* **2005**, *433* (7027), 725–728.
- (5) Fang, A. W.; Park, H.; Cohen, O.; Jones, R.; Paniccia, M. J.; Bowers, J. E. *Opt. Express* **2006**, *14* (20), 9203–9210.

- (6) Van Campenhout, J.; Rojo Romeo, P.; Regreny, P.; Seassal, C.; Van Thourhout, D.; Verstuyft, S.; Di Cioccio, L.; Fedeli, J. M.; Lagahe, C.; Baets, R. *Opt. Express* **2007**, *15* (11), 6744–6749.
- (7) Pavesi, L.; Dal Negro, L.; Mazzoleni, C.; Franzo, G.; Priolo, F. *Nature* **2000**, *408* (6811), 440–444.
- (8) Liu, J.; Sun, X.; Camacho-Aguilera, R.; Kimerling, L. C.; Michel, J. *Opt. Lett.* **2010**, *35* (5), 679–681.
- (9) Ayers, J. E. *Heteroepitaxy of Semiconductors - Theory, Growth, and Characterization*; CRC Press: Boca Raton, FL, 2007.
- (10) Sun, G.; Soref, R. A.; Cheng, H. H. *J. Appl. Phys.* **2010**, *108* (3), 033107–6.
- (11) Liebich, S.; Zimprich, M.; Beyer, A.; Lange, C.; Franzbach, D. J.; Chatterjee, S.; Hossain, N.; Sweeney, S. J.; Volz, K.; Kunert, B.; Stolz, W. *Appl. Phys. Lett.* **2011**, *99* (7), 071109–3.
- (12) Wang, Z.; Junesand, C.; Metaferia, W.; Hu, C.; Wosinski, L.; Lourduodoss, S. *Mater. Sci. Eng. B* **2012**, *177* (17), 1551–1557.
- (13) Hossain, N.; Sweeney, S. J.; Rogowsky, S.; Ostendorf, R.; Wagner, J.; Liebich, S.; Zimprich, M.; Volz, K.; Kunert, B.; Stolz, W. *Electron. Lett.* **2011**, *47* (16), 931–933.
- (14) Mårtensson, T.; Svensson, C. P. T.; Wacaser, B. A.; Larsson, M. W.; Seifert, W.; Deppert, K.; Gustafsson, A.; Wallenberg, L. R.; Samuelson, L. *Nano Lett.* **2004**, *4* (10), 1987–1990.
- (15) Guo, W.; Zhang, M.; Banerjee, A.; Bhattacharya, P. *Nano Lett.* **2010**, *10* (9), 3355–3359.
- (16) Nguyen, H. P. T.; Zhang, S.; Cui, K.; Han, X.; Fatholouloumi, S.; Couillard, M.; Botton, G. A.; Mi, Z. *Nano Lett.* **2011**, *11* (5), 1919–1924.
- (17) Tomioka, K.; Tanaka, T.; Hara, S.; Hiruma, K.; Fukui, T. *Sel. Top. Quantum Electron., IEEE J.* **2011**, *17* (4), 1112–1129.
- (18) Duan, X.; Huang, Y.; Agarwal, R.; Lieber, C. M. *Nature* **2003**, *421* (6920), 241–245.
- (19) Gradecak, S.; Qian, F.; Li, Y.; Park, H.-G.; Lieber, C. M. *Appl. Phys. Lett.* **2005**, *87* (17), 173111–3.
- (20) Johnson, J. C.; Choi, H.-J.; Knutsen, K. P.; Schaller, R. D.; Yang, P.; Saykally, R. J. *Nat. Mater.* **2002**, *1* (2), 106–110.
- (21) Chen, R.; Tran, T.-T. D.; Ng, K. W.; Ko, W. S.; Chuang, L. C.; Sedgwick, F. G.; Chang-Hasnain, C. *Nat. Photonics* **2011**, *5* (3), 170–175.
- (22) Wang, G.; Leys, M. R.; Loo, R.; Richard, O.; Bender, H.; Waldron, N.; Brammertz, G.; Dekoster, J.; Wang, W.; Seefeldt, M.; Caymax, M.; Heyns, M. M. *Appl. Phys. Lett.* **2010**, *97* (12), 121913–3.
- (23) Hiramatsu, K.; Nishiyama, K.; Onishi, M.; Mizutani, H.; Narukawa, M.; Motogaito, A.; Miyake, H.; Iyechika, Y.; Maeda, T. *J. Cryst. Growth* **2000**, *221* (1–4), 316–326.
- (24) Woo, R. L.; Xiao, R.; Kobayashi, Y.; Gao, L.; Goel, N.; Hudait, M. K.; Mallouk, T. E.; Hicks, R. F. *Nano Lett.* **2008**, *8* (12), 4664–4669.
- (25) Gerard, J.-M.; Gayral, B. *J. Lightwave Technol.* **1999**, *17* (11), 2089–2095.
- (26) Bakkens, E. P. A. M.; van Dam, J. A.; De Franceschi, S.; Kouwenhoven, L. P.; Kaiser, M.; Verheijen, M.; Wondergem, H.; van der Sluis, P. *Nat. Mater.* **2004**, *3* (11), 769–773.
- (27) Wang, G.; Leys, M. R.; Nguyen, N. D.; Loo, R.; Brammertz, G.; Richard, O.; Bender, H.; Dekoster, J.; Meuris, M.; Heyns, M. M.; Caymax, M. *J. Electrochem. Soc.* **2010**, *157* (11), H1023–H1028.
- (28) Ertekin, E.; Greaney, P. A.; Chrzan, D. C.; Sands, T. D. *J. Appl. Phys.* **2005**, *97* (11), 114325–10.
- (29) Joyce, H. J.; Wong-Leung, J.; Gao, Q.; Tan, H. H.; Jagadish, C. *Nano Lett.* **2010**, *10* (3), 908–915.
- (30) Mishra, A.; Titova, L. V.; Hoang, T. B.; Jackson, H. E.; Smith, L. M.; Yarrison-Rice, J. M.; Kim, Y.; Joyce, H. J.; Gao, Q.; Tan, H. H.; Jagadish, C. *Appl. Phys. Lett.* **2007**, *91* (26), 263104–3.
- (31) Mattila, M.; Hakkarainen, T.; Mulot, M.; Lipsanen, H. *Nanotechnology* **2006**, *17* (6), 1580.
- (32) Zhang, L.; Luo, J.-W.; Zunger, A.; Akopian, N.; Zwiller, V.; Harmand, J.-C. *Nano Lett.* **2010**, *10* (10), 4055–4060.
- (33) Pemasiri, K.; Montazeri, M.; Gass, R.; Smith, L. M.; Jackson, H. E.; Yarrison-Rice, J.; Paiman, S.; Gao, Q.; Tan, H. H.; Jagadish, C.; Zhang, X.; Zou, J. *Nano Lett.* **2009**, *9* (2), 648–654.

(34) Algra, R. E.; Verheijen, M. A.; Borgstrom, M. T.; Feiner, L.-F.; Immink, G.; van Enkevort, W. J. P.; Vlieg, E.; Bakkers, E. P. A. M. *Nature* **2008**, *456* (7220), 369–372.

(35) Bao, J.; Bell, D. C.; Capasso, F.; Wagner, J. B.; Mårtensson, T.; Trägårdh, J.; Samuelson, L. *Nano Lett.* **2008**, *8* (3), 836–841.

(36) Mohideen, U.; Slusher, R. E.; Jahnke, F.; Koch, S. W. *Phys. Rev. Lett.* **1994**, *73* (13), 1785–1788.

(37) Ates, S.; Gies, C.; Ulrich, S. M.; Wiersig, J.; Reitzenstein, S.; Löffler, A.; Forchel, A.; Jahnke, F.; Michler, P. *Phys. Rev. B* **2008**, *78* (15), 155319.

(38) Ikejiri, K.; Kitauchi, Y.; Tomioka, K.; Motohisa, J.; Fukui, T. *Nano Lett.* **2011**, *11* (10), 4314–4318.

(39) Caroff, P.; Dick, K. A.; Johansson, J.; Messing, M. E.; Deppert, K.; Samuelson, L. *Nat. Nanotechnol.* **2009**, *4* (1), 50–55.

(40) Martin, P.; Skouri, E. M.; Chusseau, L.; Alibert, C.; Bissessur, H. *Appl. Phys. Lett.* **1995**, *67* (7), 881–883.

(41) Zhang, Y.; Khan, M.; Huang, Y.; Ryou, J.; Deotare, P.; Dupuis, R.; LonCar, M. *Appl. Phys. Lett.* **2010**, *97* (5), 051104–3.